Computers & Geosciences 183 (2024) 105508

Contents lists available at ScienceDirect

Computers and Geosciences

journal homepage: www.elsevier.com/locate/cageo

Research paper

Physics-informed surrogate modeling for supporting climate resilience at groundwater contamination sites

Aurelien Meray [a,*,1], Lijing Wang [b,1], Takuya Kurihana [c], Ilijana Mastilovic [d], Satyarth Praveen [b], Zexuan Xu [b], Milad Memarzadeh [e], Alexander Lavin [f], Haruko Wainwright [g]

[a] Knight Foundation School of Computing and Information Sciences, Florida International University, Miami, FL 33199, United States of America
[b] Lawrence Berkeley National Laboratory, Berkeley, CA 94720, United States of America
[c] Department of Computer Science, University of Chicago, Chicago, IL 60637, United States of America
[d] School of Freshwater Sciences, University of Wisconsin - Milwaukee, Milwaukee, WI 53204, United States of America
[e] NASA Ames Research Center, Mountain View, CA 94035, United States of America
[f] Pasteur Labs & ISI, Brooklyn, NY 11205, United States of America
[g] Department of Nuclear Science and Engineering, Department of Civil and Environmental Engineering, Massachusetts Institute of Technology, Cambridge, MA 02139, United States of America

ARTICLE INFO

Dataset link: https://console.cloud.google.com/storage/browser/us-digitaltwiner-pub-features/srs_farea_ensemble_simulations_dataset

Keywords:
Soil and groundwater contamination
Physics-informed machine learning
U-Net Enhanced Fourier Neural Operator (U-FNO)
Groundwater contamination
Boundary condition loss function
Supercomputer
U-FNOB
U-FNOB-R
Physics situations

ABSTRACT

Contamination of soil and groundwater presents a widespread global problem, significantly impacting both human well-being and environmental stability. Conventional models employed for estimating pollutant concentrations under varying climatic conditions demand extensive computational power and high-performance computing resources. In response to this issue, we have devised an innovative method utilizing a physics-informed machine learning technique, known as the U-Net Enhanced Fourier Neural Operator (U-FNO), to generate rapid surrogate models for flow and transport. These models are capable of forecasting groundwater pollution levels under diverse climatic situations and subsurface characteristics without necessitating a supercomputer. In our research, we centered our attention on the Department of Energy's Savannah River Site (SRS) F-Area and established two time-dependent structures: U-FNOB and U-FNOB-R. Both frameworks incorporate a tailored loss function, including specific physical constraints of groundwater flow and transport such as spatial derivatives, and contaminant boundary conditions. The findings of our study indicate that the U-FNO models can consistently foresee spatialtemporal fluctuations in groundwater flow and pollutant transportation properties, such as contaminant concentration, hydraulic head, and Darcy's velocity. Our research reveals that the U-FNOB-R architecture is especially adept at predicting the effects of alterations in recharge rates on groundwater contamination sites, delivering superior time-dependent forecasts compared to the U-FNOB structure. Our novel approach holds the potential to revolutionize environmental monitoring and remediation efforts by providing rapid, precise, and cost-efficient estimations of groundwater pollution levels under uncertain climate conditions.

1. Introduction

Groundwater contamination is a pervasive problem that affects humans and the environment worldwide. In the United States, 130 million people rely on groundwater for drinking water, but one of every five wells (22% out of 6600 wells) sampled in the part of aquifers used for drinking water exceeds the safe contaminant level for human health (Desimone et al., 2014). Groundwater contamination sites present a range of health and environmental risks because of their large size, prominence, and contamination with harmful chemicals as a result of various industrial operations, such as mining, nuclear weapon production, chemical plants, or intensive agricultural activities. These toxic substances can enter surrounding ground or surface water and contaminate drinking water reservoirs. Contamination sites are often remediated through various engineering treatments such as pump-and-treat (Mackay and Cherry, 1989), in-situ treatment (Nyer, 2000), or monitored natural attenuation (Clement et al., 2002). However, contamination plumes remain in the subsurface for an extended time, and/or the residual contaminants in the unsaturated zone often require long-term monitoring (Schmidt et al., 2018; Denham et al., 2020;

* Corresponding author.
E-mail address: amera009@fiu.edu (A. Meray).
[1] These authors contributed equally and share co-first authorship.

https://doi.org/10.1016/j.cageo.2023.105508
Received 7 May 2023; Received in revised form 28 November 2023; Accepted 8 December 2023
Available online 14 December 2023

Meray et al., 2022) in order to control the risks to humans and the environment.

Climate change causes more challenges in contamination site remediation. The frequency of extreme precipitation events, such as heavy rains or prolonged droughts, has already increased globally (Katz and Brown, 1992; Orlowsky and Seneviratne, 2012; Rahmstorf and Coumou, 2011), which can change the water balance spatiotemporally. Water balance changes in each local scale can impact the plume mobility or remobilize the contaminants with increased infiltration or groundwater gradient change. Such future impacts can be assessed by simulating groundwater flow and contaminant transport to predict contaminant concentrations in different climate scenarios (Libera et al., 2019; Xu et al., 2022). Libera et al. (2019) studies the effect of increased precipitation using a groundwater model and found that it causes dilution in the system immediately after but ultimately leads to contaminant concentration increases. Xu et al. (2022) further investigates the water balance impact using the downscaled climate projection data (CMIP5) as the input for the reactive transport model and evaluates the impact on contaminants with uncertain hydrologic shifts.

However, these physical simulations are often time-consuming and require us to run new simulations with every uncertain climate scenario on high-performance computers (HPC). Although Libera et al. (2019) and Xu et al. (2022) used groundwater flow and transport models, they performed scenario-based studies without full uncertainty quantification. In addition, they did not address the uncertainty in subsurface parameters, and their effect on the climate change impacts. Such simulations are very computationally expensive to run. Site managers and practitioners need a fast evaluation tool for examining the potential effects of many climate projections on the fate and transport of contaminants.

Recent advances in machine learning (ML) have demonstrated the capability to rapidly emulate physical simulations and directly solve partial differential equations (PDEs) (Lu et al., 2019; Li et al., 2020). A widely recognized method, known as *neural operator learning*, employs neural networks to acquire mesh-independent, resolution-invariant solution operators for PDEs, with training necessitating only simulation data rather than precise governing PDE equations. Li et al. (2020) introduced the Fourier Neural Operator (FNO), a neural operator formulated in infinite-dimensional Fourier spaces. Operating within the Fourier domain, FNO provides resolution-invariant solutions and exhibits robustness against high-frequency noise. FNO has been successfully applied to various flow dynamics problems, including Darcy's flow, Burger's equation, Navier–Stokes equation, and multi-phase flow (Li et al., 2020; Zhang et al., 2022). In an attempt to enhance FNO, Wen et al. (2022) incorporated a U-Net architecture (Ronneberger et al., 2015) and proposed U-FNO, a U-Net augmented version designed to emulate ensemble simulations of spatiotemporal image-like outputs. Despite the loss of flexibility in training with different resolution data, U-FNO achieved lower training and test errors for multi-phase flow predictions. The Physics-Informed Neural Network (PINN) framework has emerged as an alternative for emulating PDE-based simulations using limited training data while maintaining high accuracy (Raissi et al., 2019; He and Tartakovsky, 2021; Li et al., 2021; Haghighat et al., 2022). PINN incorporates simulation data, governing relations, and initial as well as boundary conditions within the neural network loss functions. By enforcing additional loss functions with physical laws, the PINN framework can learn PDE solutions more quickly and accurately.

In this paper, we show how to build a class of multiphysics emulator based on Neural Operator learning (Li et al., 2020; Lavin et al., 2021; Wen et al., 2022) in order to effectively model groundwater flow and contaminant transport in real-world environments. Effective, in this case, goes beyond physical accuracy and reliability in generalization: our approach addresses the most significant bottleneck in this area of climate and Earth systems, by eliminating the need to run many individual physics simulations, which are prohibitively expensive computationally, and far too time-consuming to robustly assess contaminant impacts on the environment. We design two architectures to emulate the flow and transport model: U-FNOB-R and U-FNOB, which have different architectures to address the time dependency of contaminant transport. We also compare these two architectures in evaluating the time-varying impacts of water balance. Inspired by PINN, we introduce multiple loss functions under a data-driven framework and consider physical boundary constraints in our machine-learning surrogate model. We apply this method using the groundwater model developed for a live site: the Savannah River Site (SRS) F-Area. With the architectures described here, validated on real operational data, we provide a computationally-efficient, lightweight approach to emulating spatiotemporal variations of groundwater contamination, capable of distributed computing, running on personal computers, and iterating through magnitudes more experiments to explore different options and conditions, all with potential for decision-making in critical climate scenarios.

2. Methodology

In this section, we present two neural network architectures, U-FNOB and U-FNOB-R, designed to build a surrogate model for groundwater flow and transport physical simulations. Both maintain fundamentally similar architecture as their base model, the U-Net enhanced Fourier Neural Operator (U-FNO). The distinction lies in the introduction of boundary conditions within the loss functions of both U-FNOB and U-FNOB-R, hence the added "B". For completeness, we include descriptions of the Fourier Neural Operator (Li et al., 2020), U-Net enhanced FNO (Wen et al., 2022), and hybrid physics-based (Raissi et al., 2019). We then highlight our approach to handling boundary conditions in the loss functions of U-FNOB and U-FNOB-R for our surrogate model training.

2.1. Neural network architectures

2.1.1. Fourier neural operator and U-Fourier layer

The goal of Fourier Neural Operator (FNO) (Li et al., 2020) is to learn mappings between infinite-dimensional spaces from input–output pairs. In our example, the input–output pairs are $m(\mathbf{x},t)$ and $y(\mathbf{x},t)$ defined in 2D spatial domain $\mathbf{x}_i$ and time t_i. FNO transfers the function $v_j(\mathbf{x},t)$ into the Fourier domain $(\mathcal{F}(v_j))(\mathbf{x},t)$, where $v_j(\mathbf{x},t)$ is an intermediate function after multiple layers applied to $m(\mathbf{x},t)$. $v_1, v_2, \ldots, v_j, \ldots$ is a sequence of architectures, where j indicates the architecture index. FNO then performs a linear transformation R in the Fourier frequency domain, and inversely transforms $\mathcal{F}^{-1}$ from the Fourier domain to the spatiotemporal domain. The entire transformation from one Fourier layer is:

$$v_{j+1}(x,t) \leftarrow \sigma\Big(\mathcal{F}^{-1}\big(R \cdot \mathcal{F}(v_j)\big)(\mathbf{x},t) + W v_j(\mathbf{x},t)\Big) \tag{1}$$

σ is the activation function. Here in this work, we use the Gaussian Error Linear Units (GELU) activation function from Hendrycks and Gimpel (2016). W is an additional linear transformation on the v_j function space. We can use the Fourier frequency modes to represent any resolution for inputs and outputs because the Fourier basis is defined in everywhere of $\mathcal{R}^{d_m}$.

U-FNO is a U-Net enhanced version of FNO and adds an additional U-Net architecture: $\mathcal{U}$ for each Fourier layer. Then one U-Fourier layer does:

$$v_{j+1}(x,t) \leftarrow \sigma\Big(\mathcal{F}^{-1}\big(R \cdot \mathcal{F}(v_j)\big)(x,t) + \mathcal{U}(v_j)(x,t) + W v_j(x,t)\Big) \tag{2}$$

Although this additional U-Net convolutional mapping loses the FNO's flexibility on training with data in different resolutions, it improves lower training/test error for multi-phase flow predictions (Wen et al., 2022). U-FNO architecture has iterative Fourier layers followed by iterative U-Fourier layers. Then with additional fully connected

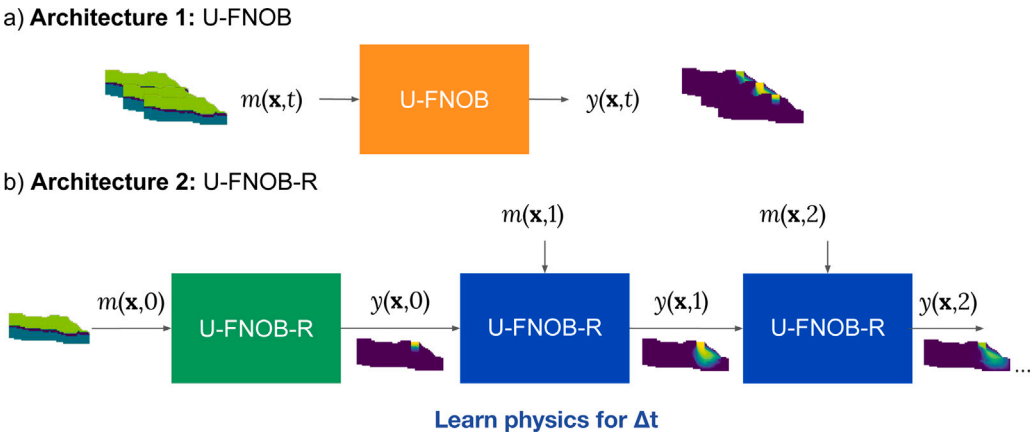

Fig. 1. U-FNO architectures: U-FNOB and U-FNOB-R.

neural network P, Q as the first and the last layer, the final U-FNO architecture is:

$$m(\mathbf{x},t) \mapsto P\big(m(\mathbf{x},t)\big) = v_{l_0}(\mathbf{x},t) \mapsto \ldots \mapsto v_{l_L}(\mathbf{x},t) \mapsto v_{k_0}(\mathbf{x},t) \mapsto \ldots \mapsto v_{k_K}(\mathbf{x},t) \mapsto Q(v_{k_K}(\mathbf{x},t)) = \hat{y}(\mathbf{x},t) \tag{3}$$

L is the number of Fourier layers, K is the number of U-Fourier layers.

2.1.2. Architectures: U-FNOB and U-FNOB-R

In the present study, we develop a pair of distinct neural operator frameworks: U-FNOB and U-FNOB-R, which are designed to forecast spatialtemporal contaminant concentrations and characteristics of groundwater flow, based on the U-Net enhanced FNO architectures. Our two architectures address the temporal dimension differently.

$$\hat{y}(x,t) = f_{\text{U-FNOB}}\big(m(x,0),\ldots,m(x,t),m(x,t+1),\ldots,m(x,T)\big), t = 1,2,\ldots,T \tag{4}$$

$$\hat{y}(x,t) = f_{\text{U-FNOB-R}}\big(m(x,0),\ldots,m(x,t)\big), t = 1,2,\ldots,T \tag{5}$$

U-FNOB, as described in Eq. (3) or its simplified counterpart in Eq. (4), integrates all input time-series data and concurrently predicts transient output characteristics (Fig. 1a). Conversely, U-FNOB-R in Eq. (5) yields output $\hat{y}(x,t)$, contingent solely upon input up to and including time t (Fig. 1b).

U-FNOB encompasses Fourier and U-Fourier layers applicable to three-dimensional spaces, which consist of two spatial dimensions and a single temporal dimension. In contrast, U-FNOB-R carries out Fourier transformations and U-Net convolutions exclusively within the 2D spatial domain, and perpetuates recurrently through time (Li et al., 2020). For each time instance t, the input and output take the form $m(x,t)$, $y(x,t-1)$ and $y(x,t)$, respectively. The input for $t+1$ incorporates an additional element: the output from the preceding step t. U-FNOB-R acquires the physical properties between every fixed time interval Δt, where Δt is equivalent to five years. As the initial stage $t = 0$ for U-FNOB-R lacks predictions from prior steps, an alternative U-FNOB-R model is trained (the green block in Fig. 1b) specifically for the initial stage $t = 0$, utilizing input $m(x,0)$ and output $y(x,0)$.

The most significant benefit of employing U-FNOB-R lies in its ability to distinctly represent temporal dependencies within the context of the recurrent network. In U-FNOB, the time domain has been included in all convolutions and Fourier transformations, then the input parameters at any time, even after t, impact $\hat{y}(x,t)$. For example, if we want to investigate how future recharge rates change plume mobilizations, then logically, the previous contaminant concentration should stay the same, only the future concentration change. In the Results and Discussion section, we will test the trained surrogate model with varying future recharge rates and present the differences between using U-FNOB and U-FNOB-R. Additionally, U-FNOB has a huge set of parameters to train while the U-FNOB-R has only $\frac{2}{T}$ of U-FNOB parameters.

However, this additional time dependency in U-FNOB-R makes its training practically harder and takes a longer time. There are accumulated errors through the recurrent neural network. U-FNOB-R has also less flexibility in time discretization: $[0,T]$ is discretized into time snapshots $t_0, t_1 \ldots, t_T$ with the same time interval $t_{i+1} - t_i = \Delta T$. In U-FNOB, $[0,T]$ is discretized arbitrarily into any time snapshots $t_0, t_1 \ldots, t_T$. Additionally, U-FNOB only needs inference once to predict a time series of plumes, while U-FNOB-R needs many recurrent inferences.

2.2. Combining physics-based and data-driven loss functions

We present four distinct loss functions incorporating both data-driven components and physical boundary constraints. Our surrogate model generates predictions $\hat{y}(\mathbf{x},t) = \hat{h}(\mathbf{x},t), \hat{q_x}(\mathbf{x},t), \hat{q_z}(\mathbf{x},t), \hat{c}(\mathbf{x},t)$. The ground truth $y(\mathbf{x},t)$ stems from Amanzi numerical solver results. Consequently, the devised loss functions address both the data-driven discrepancies between predictions $\hat{y}(\mathbf{x},t)$ and $y(\mathbf{x},t)$ and, more intriguingly, the physical constraints inherent in solving PDEs, such as boundary conditions.

Mean relative error: Initially, we evaluate the data-driven discrepancy by employing the mean relative error (MRE), which considers the ℓ_2 norm:

$$\mathcal{L}_{MRE}(y,\hat{y}) = \frac{\|y-\hat{y}\|_2}{\|y\|_2}. \tag{6}$$

Spatial derivatives: We also account for the first derivatives in the horizontal direction x and the vertical direction z. These spatial derivatives enable us to match not only the output values but also their derivatives. It is worth noting that factors such as the hydraulic head primarily influence flow and transport, rather than the actual values.

$$\mathcal{L}_{der}(y,\hat{y}) = \frac{\|\partial y/\partial x - \partial \hat{y}/\partial x\|_2}{\|\partial y/\partial x\|_2} + \frac{\|\partial y/\partial z - \partial \hat{y}/\partial z\|_2}{\|\partial y/\partial z\|_2}. \tag{7}$$

Indeed, these spatial derivatives encompass the output's actual values. Eqs. (7) and (6) are not mutually exclusive.

Spatial derivatives on the contaminant boundary: The Maximum Contaminant Level (MCL), as recommended by the Environmental Protection Agency (EPA) (Libera et al., 2019), denotes the highest permissible concentration of a contaminant in drinking water. Accordingly, predicting contaminant boundaries exceeding the MCL is crucial for site managers to safeguard water resources. We incorporate the first derivatives on the contaminant boundary, where $c \geq MCL$. These first

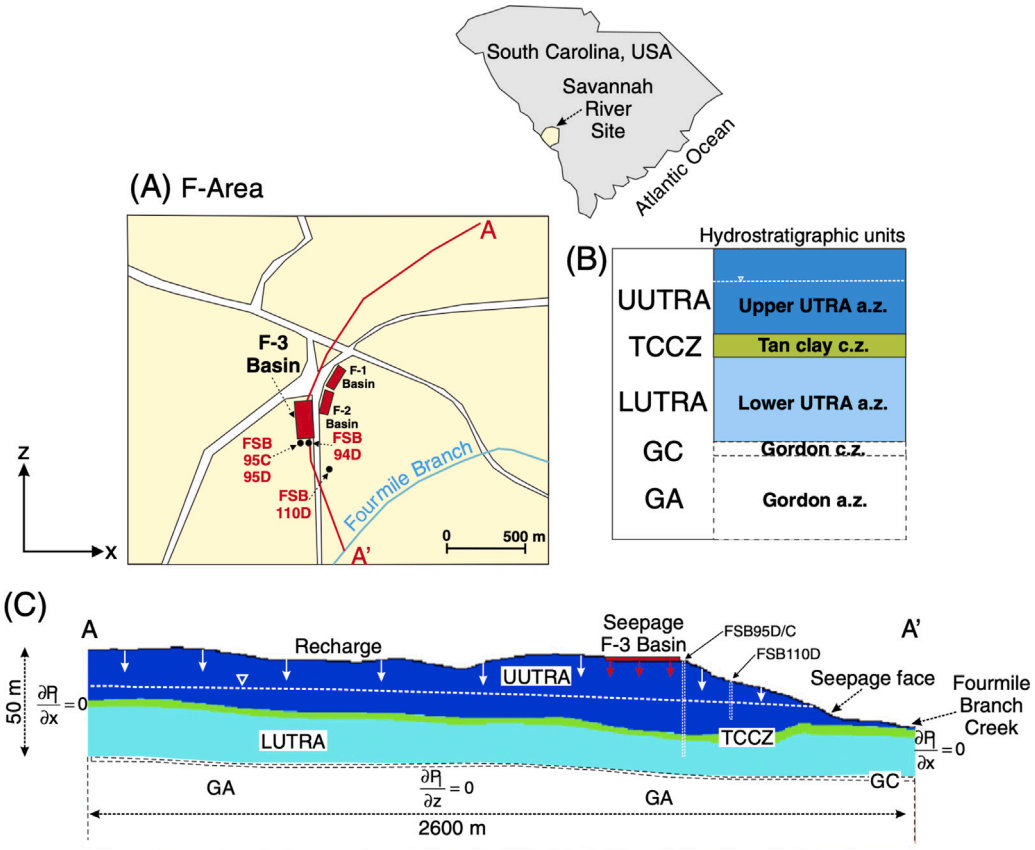

Fig. 2. (a) Geographical positioning of leakage basins (F1, F2, F3) within the F-Area at SRS, South Carolina; (b) Hydrostratigraphic divisions established for the F-Area; (c) Two-dimensional cross-sectional representation of the model domain. These figures have been sourced from the studies conducted by Bea et al. (2013) and Xu et al. (2022).

derivatives have high values at the boundary and zero values for the rest of the 2D domain.

$$\mathcal{L}_{conc}(y,\hat{y}) = \frac{\|\partial c'/\partial x - \partial \hat{c'}/\partial x\|_2}{\|\partial c'/\partial x\|_2} + \frac{\|\partial c'/\partial z - \partial \hat{c'}/\partial z\|_2}{\|\partial c'/\partial z\|_2},$$
$$\text{where } c' = \begin{cases} 0, & c < MCL \\ 1, & c \geq MCL \end{cases}, \quad \hat{c'} = \begin{cases} 0, & \hat{c} < MCL \\ 1, & \hat{c} \geq MCL \end{cases} \tag{8}$$

Physics-informed boundary conditions: We add no-flow boundary condition constraints in loss functions using physics-informed neural networks (Raissi et al., 2019) to help solve the PDEs. In Amanzi physical simulations, no-flow boundary conditions are assigned along the two vertical sides because of the groundwater divides, where assuming topographic prevents any regional groundwater flux, and also assigned along the bottom of the computational domain because of the impermeable clay-rich layer at the bottom (Xu et al., 2022). The additional no-flow boundary loss function helps the surrogate model learn these boundary constraints. We denote the boundary of the spatial domain D as ∂D.

$$\mathcal{L}_{BC}(\hat{y}) = \|\hat{q}_x|_{\partial D}\|_2 + \|\hat{q}_z|_{\partial D}\|_2 + \|\partial \hat{h}|_{\partial D}\|_2 \tag{9}$$

Composite loss function: The composite loss function integrates all the previously defined loss functions, each associated with its respective hyperparameter β.

$$\mathcal{L}(y,\hat{y}) = \mathcal{L}_{MRE}(y,\hat{y}) + \beta_1 \mathcal{L}_{der}(y,\hat{y}) + \beta_2 \mathcal{L}_{conc}(y,\hat{y}) + \beta_3 \mathcal{L}_{BC}(\hat{y}) \tag{10}$$

3. Application

In this section, we apply our study's findings to a real-world context, focusing on the groundwater system at the Department of Energy's SRS F-Area in South Carolina. We provide an in-depth description of the case study, discuss the data transformation and model training process, and evaluate different model architectures and loss functions. We also highlight the computational efficiency of our approach and present predictions for transient flow and transport properties. Lastly, we assess the adaptability of groundwater contamination sites to changing recharge rates, emphasizing the practical implications of our research in the context of climate change and environmental response.

3.1. Description of the case study

We used the same model and domain setting as Libera et al. (2019) and Xu et al. (2022). This model was established for the groundwater system at the Department of Energy's (DOE) SRS F-Area, depicted in Fig. 2. Situated in South Carolina, the SRS F-Area spans approximately 800 km^2 and is located around 100 miles from the Atlantic Ocean. During the Cold War era, this site played a crucial role in the production of specific radioactive isotopes, such as tritium, uranium, and cesium-137. The disposal of low-level radioactive waste was carried out in three distinct basins, namely F-1, F-2, and F-3, during the period from 1955 to 1988. Subsequently, in 1988, these basins were sealed with a low-permeability material.

The hydrostratigraphy of the SRS F-Area comprises three units: an upper aquifer zone, a tan clay confining zone, and a lower aquifer zone. Historical monitoring data indicates that contaminants from the waste have affected both the upper and lower aquifer zones, which are interconnected. The Amanzi model, as described in Libera et al. (2019) and Xu et al. (2022), is designed to simulate a 2D cross-section of the SRS F-Area, incorporating the F-3 basin. The 2D cross-section (Fig. 3) measures approximately 2600 m in length and 100 m in depth, representing a cross-section at the center of the SRS's F-3 basin. The horizontal grid resolution along the cross-section is set at 10 m, while

Table 1
Parameters of the physical model employed in flow and transport simulations. $U(a, b)$ denotes the uniform distribution with the minimum value a and the maximum value b. For different physical simulations, we draw distinct model parameters from these uniform distributions.

Hydrostratigraphic unit	Upper aquifer	Tan clay	Lower aquifer
Porosity (–)	$U(3.1e-1, 4.7e-1)$	0.39	0.39
Permeability (m^2)	$U(2.5e-12, 7.5e-12)$	1.98e–14	5e–12
α (–)	$U(3.2e-4, 4.8e-4)$	5.1e–5	5.1e–5
Residual water content [Sr] (–)	$U(1.4e-1, 2.2e-1)$	0.39	0.41
m (–)	$U(4e-1, 6e-1)$	0.5	0.5
Source concentration (mol/L)	$U(1e-9, 1e-8)$	–	–
Infiltration rate before the cap (kg-water m^{-2} s^{-1})	$U(1e-4, 2.5e-4)$	–	–
Infiltration rate after the cap (kg-water m^{-2} s^{-1})	$U(2e-9, 1e-8)$	–	–
Time-varying recharge (kg-water m^{-2} s^{-1})	$U(2e-6, 2e-5)$	–	–

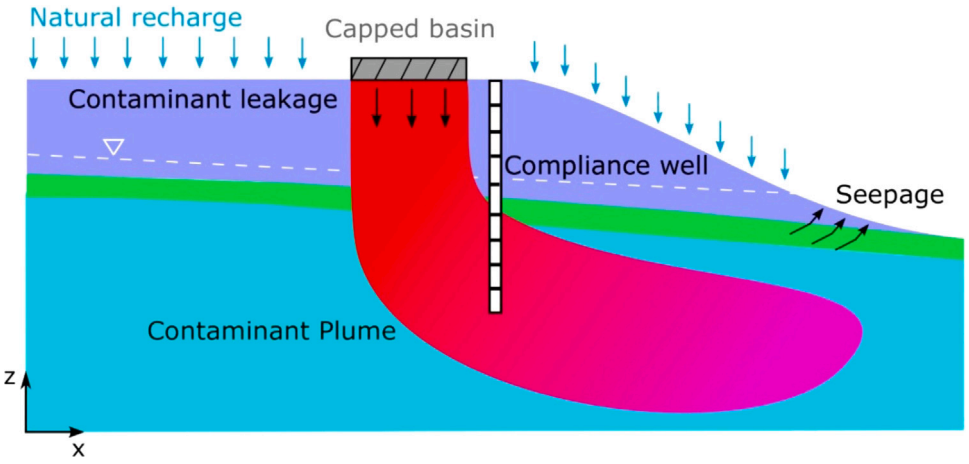

Fig. 3. Depiction of the hydrological model employed in the physical simulations at the SRS, presenting a vertical two-dimensional cross-section through the central axis of the contamination origin area.
Source: Adapted from Xu et al. (2022).

the vertical discretization comprises 48 layers, with thicknesses ranging from 0.15 m to 1.86 m.

To construct the surrogate model for this study, we utilized Amanzi, a solver for groundwater flow and advection–dispersion transport equations that enables simulation of both unsaturated and saturated flow. The Amanzi model used in this experiment is identical to the one described in Libera et al. (2019), and it simulates groundwater flow and tritium transport and decay processes.

We conducted 1000 simulations, incorporating both climate and subsurface uncertainties. To address the subsurface uncertainties, we employed random sampling from a uniform distribution for each parameter. The uncertainties in climate and subsurface parameters are represented by uniform distributions listed in Table 1. We implemented climate uncertainty by introducing periodic recharge rates from 1954 to 2100, which differ across three periods: historical (1954–2020), mid-century (2020–2060), and late-century (2060–2100). We inferred and amplified the uniform distribution of recharge rates $U(2e-6, 2e-5)$ kg-water m^{-2} s^{-1} in Table 1 based on (1) the historical recharge rate estimate presented in Bea et al. (2013) and (2) the recharge distributions from various climate projections (RCP 2.6, RCP 4.5, RCP 6.0, RCP 8.5) in CMIP5 (Knutti and Sedláček, 2013). The subsurface parameters include porosity and permeability for the upper aquifer, inverse air entry suction (denoted as α), residual water content, and the measure of the pore-size distribution (indicated as m) in the van Genuchten water retention curve. Additional parameters accounted for are the infiltration rate uncertainty at the F-3 basin both before and after 1988, along with an indeterminate tritium concentration in the infiltrating water, represented as the source concentration. The Amanzi model could encounter numerical convergence issues, potentially leading to unsuccessful simulations.

It was observed that failures in the Amanzi model were primarily due to combinations of unrealistic recharge parameters and low permeabilities, creating unfeasible conditions. As a result, simulations presenting such scenarios were filtered out, maintaining focus on relevant, realistic scenarios and enhancing the reliability of our results. The decision to run a total of 1000 simulations was optimized based on available computational resources —providing an adequate exploration of the parameter space while maintaining robustness of the model. This resulted in the completion of 664 successful simulations, thereby ensuring compliance with the conditions mentioned and constituting the basis for this project.

3.2. Input and outputs for surrogate model training

In this investigation, our data consist of specific input and output variables. The input involves uncertain physical model parameters, denoted as $m(\mathbf{x}, t)$, and mentioned in Table 1. The output, represented by $y(\mathbf{x}, t)$, reflects the site's two-dimensional cross-section incorporating the spatiotemporal flow and transport properties. The output is therefore expressed as follows: $y(\mathbf{x}, t) = q_x(\mathbf{x}, t), q_z(\mathbf{x}, t), h(\mathbf{x}, t), c(\mathbf{x}, t)$

Here, $q_x(\mathbf{x}, t)$ and $q_z(\mathbf{x}, t)$ denote Darcy's velocity in the x and z directions, respectively, while $h(\mathbf{x}, t)$ signifies the hydraulic head and $c(\mathbf{x}, t)$ denotes the tritium concentration. The $\mathbf{x}$ in $y(\mathbf{x}, t)$ symbolizes the location vector within the 2D spatial cross-section, oriented along the x-axis and z-axis, while t earmarks the temporal variable from 1954 to 2100.

To optimize these input and output variables for machine learning surrogate model training, we apply a series of transformations. We re-grid the output layers into a uniform discretization, with a 10-m resolution on the x-axis and a 2.5-m resolution on the z-axis. Consequently, we obtain 257×24 cells in the x and z directions, respectively. The scalar input variables are broadcasted into the output size to guarantee the same dimensional shape for the inputs and outputs. Constant values in the Tan Clay and the Lower Aquifer, as well as

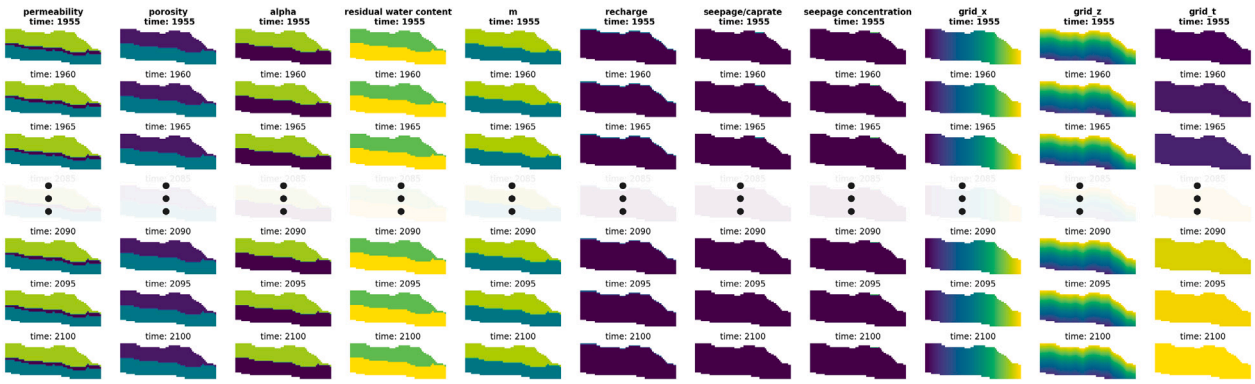

Fig. 4. Spatially imputed inputs with 11 different variables.

uncertain values in the Upper Aquifer, are filled into different layers of the cross-section. These layers can be seen in the first five columns of Fig. 4.

Furthermore, we merge time-varying recharge rates in history (1954–2020), mid-century (2020–2060), and late-century (2060–2100) into one channel, and impute the recharge rate only at the top cell of the 2D cross-section. This same transformation applies to the seepage rate and cap rate at the top cells within the seepage basin, where the seepage rate only applies before 1988 and the cap rate only after 1988. Lastly, the horizontal and vertical locations of the grid, along with the timestamp, are encoded (represented as grid_x, grid_z, and grid_t). With these transformations, the final dimensional shape for each input sample $m(\mathbf{x}, t)$ can be represented as (nz, nx, nt, nc), such that nz is the size of z, nx is the size of x, nt is the number of time steps, and nc is the number of encoded parameters. This results in our $664 \times (24, 257, 30, 11)$ input shape.

In a similar vein to the input, we transform the output save for the final dimension, which stands for the quantity of predicted output parameters. Consequently, the output $y(\mathbf{x}, t)$ shape takes on the (nz, nx, nt, no) form. This results then in our adopted output format of $664 \times (24, 257, 30, 4)$. After the transformations mentioned above, we then standardize our data to make it suitable for our machine learning model. Given the heterogeneous nature of the input and output variables, we apply MinMax scaling uniquely to each variable. This step normalizes the range for all variables, ensuring uniformity and limiting the influence of high-magnitude variables. Therefore, each variable in both the input and the output data is scaled individually to have a range between 0 and 1. This operation is critical not only for maintaining the integrity of each variable's dynamics but also for easing and enhancing the models' learning and convergence process.

3.3. Performance of different architectures and loss functions

In this study, we conducted a series of experiments to evaluate and compare the performance of different architecture configurations and loss functions. All experiments used the same training set, which consisted of 80% of Amanzi simulations. A separate 10% of the simulations was reserved for validation during the training process, while the remaining 10% served as the test set for later model performance evaluation. These distinct datasets ensured consistency and fairness across all experiments.

The various experiments were designed to systematically compare and optimize architectures, as well as loss function components. The initial experiments compared the performance of Fourier Neural Operator (FNO) with two different architectures (FNO-2D and FNO-3D) and the proposed U-FNOB and U-FNOB-R architectures with zero hyperparameters for the loss function components (meaning, $\beta_1 = \beta_2 = \beta_3 = 0$) in Eq. (10). FNO-2D and FNO-3D, as brought forth by Li et al. (2020), utilizes Fourier theory to resolve partial differential equations. Specifically, FNO-2D denotes a 2-D Fourier neural operator structured around a recurrent neural network (RNN) in time, while FNO-3D points to a 3-D Fourier neural operator directly convolving in the space–time continuum. These initial comparisons demonstrated the performance improvement brought on by the proposed U-FNOB and U-FNOB-R architectures.

Second, as we sought to optimize the loss function, different combinations of non-zero hyperparameters $\beta_1, \beta_2, \beta_3$ were tested with our proposed U-FNOB architecture. The intention of this experiment was to find the optimum balance of these hyperparameters that would yield the lowest prediction error. Table 2 includes the results from all experiments, for consistency and transparency. It includes the mean relative error (MRE) and mean squared error (MSE) values obtained from the validation data across these different experiments — the baseline FNO-2D and FNO-3D, the proposed U-FNOB and U-FNOB-R architectures with zero hyperparameters in loss functions, and then the various configurations of non-zero hyperparameters for the loss functions with the U-FNOB architecture.

Finally, having decided on the best-performing architecture (U-FNOB) and the optimized loss function (with $\beta_1 = \beta_2 = \beta_3 = 0.1$), we did further training for a higher number of epochs (150 in total). Here, only U-FNOB and U-FNOB-R architectures were tested against the test data with optimized hyperparameters substituting into Eq. (10). The resulting performances of this final set of models are presented in Table 2 at experiment 9 and 10.

This robust approach allowed us to effectively compare and benchmark the results, showcasing that the best performance was achieved by implementing the U-Net architecture in conjunction with our proposed hybrid loss function, which considered all spatial derivatives and no flow boundaries. Moreover, the results validated the importance of both an effective architecture and a carefully tailored loss function for optimal surrogate model building for physical simulations (see Fig. 5).

3.4. Computational efficiency

Efficiency is central to our proposed approach in simulating groundwater flow and transport. Although the initial stages of the process – simulation and model training – require an upfront computational commitment, the ultimate benefit is found in the accelerated speed of simulation reproductions made possible once these stages are complete. This efficiency trade-off is further illustrated in Fig. 6, where the total computational time for different numbers of simulation runs is compared between the traditional numerical simulator and our models.

Each simulation takes on average about 8.9 min. This is less of a burden than it might appear, as there are ample opportunities for parallelization, contributing to significant time efficiency. Training the U-FNOB architecture takes approximately 72 min for 30 epochs. Comparatively, using the U-FNOB-R architecture requires a lengthier 273 min, making the U-FNOB approximately four times faster.

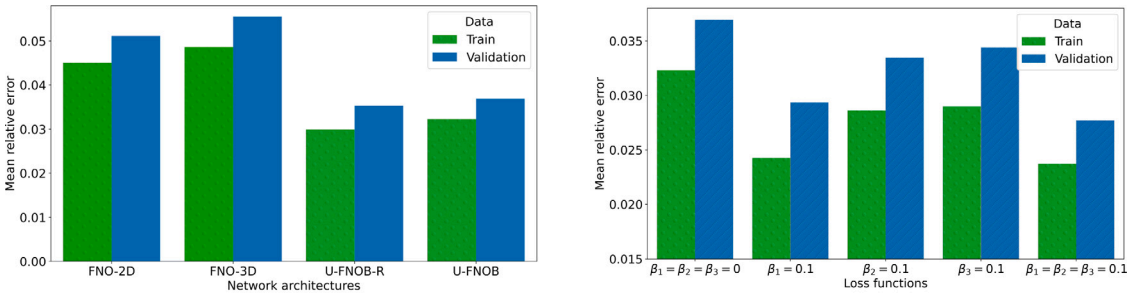

Fig. 5. Mean relative errors for different architectures and loss functions. (a) Comparison between U-FNO and FNO. (b) Comparison between different loss functions. $\beta_1, \beta_2, \beta_3$ are the hyperparameters in Eq. (10). All experiments in (a) and (b) were trained for 30 epochs. (a) have all $\beta_1 = \beta_2 = \beta_3 = 0$, (b) are trained on U-FNOB. Note: If only one beta value is shown, the other betas are set to zero.

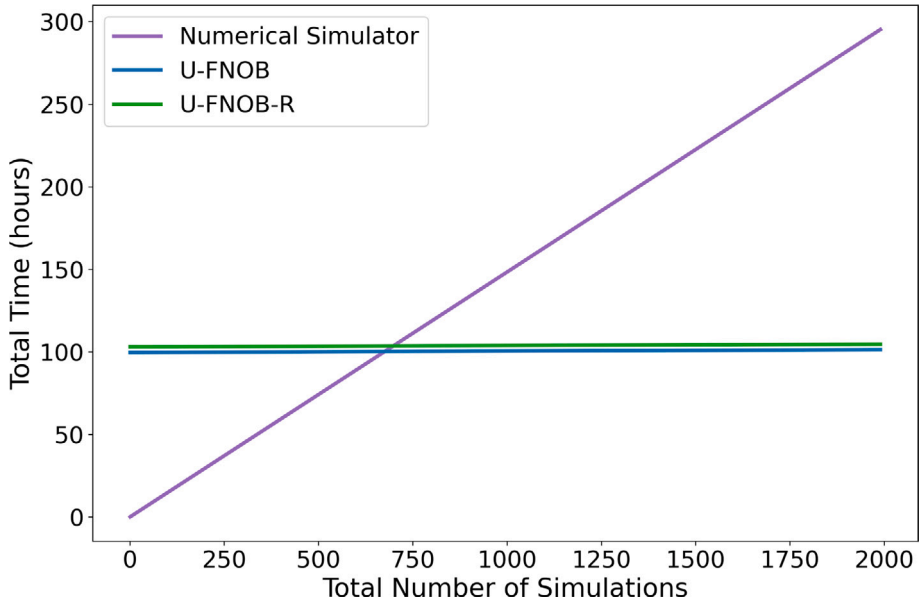

Fig. 6. Trade-Off between Numerical Simulator and Machine Learning Approaches (U-FNOB & U-FNOB-R). The computational times depicted include the respective methods of the numerical simulator and the machine learning model generation process. For the ML models, the assigned times incorporate the average time for dataset collection (664 simulations), model training time, and inference. Despite these more substantial initial time investments, ML models show increased efficiency for larger scale simulations.

Table 2
Evaluation of mean relative errors (MRE) and mean squared errors (MSE) across all experiments conducted.

Experiment	Architectures	Epochs	Loss $(\beta_1, \beta_2, \beta_3)$	MRE	MSE	Evaluation on
1	FNO-2D	30	(0,0,0)	0.051	2.71e−4	Validation
2	FNO-3D	30	(0,0,0)	0.055	2.98e−4	
3	U-FNOB-R	30	(0,0,0)	**0.035**	**1.51e−4**	
4	U-FNOB	30	(0,0,0)	**0.037**	**1.29e−4**	
5	U-FNOB	30	(0.1,0,0)	0.029	8.83e−5	
6	U-FNOB	30	(0,0.1,0)	0.033	1.10e−4	
7	U-FNOB	30	(0,0,0.1)	0.034	1.27e−4	
8	U-FNOB	30	(0.1,0.1,0.1)	**0.028**	**8.14e−5**	
9	U-FNOB-R	150	(0.1,0.1,0.1)	0.020	4.49e−5	Test
10	U-FNOB	150	(0.1,0.1,0.1)	**0.014**	**2.44e−5**	

Herein lies the value of the upfront computational investment. Upon completion of the model training, the rapid computation capability of the trained models comes into play. These models significantly curb both the time requirement and computational cost when generating output. Specifically, the inference time on these models averages less than a second, enabling the fast generation of a large volume of data across various input parameters.

Taken together, this process offers an extremely efficient way to simulate groundwater flow and transport, combining the speed of the U-FNOB architecture with the prowess of trained models. As demonstrated in Fig. 6, the resulting process provides not only a significant reduction in computational demand but also a speedy output generation, a critical attribute when planning for and responding to environmental changes.

3.5. Predicting transient flow and transport properties

In this study, we predict four key flow and transport properties, including Darcy's velocity in the x and z directions, hydraulic head,

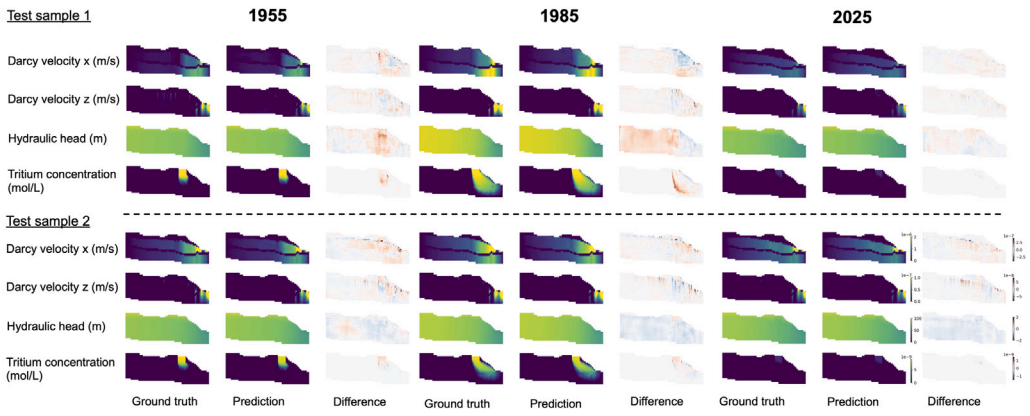

Fig. 7. Flow and transport properties predictions with U-FNOB, Index 10 in Table 2. Specific input parameters used for this sample, consisting of subsurface and climate variables, are detailed in the supplementary material Table S1.

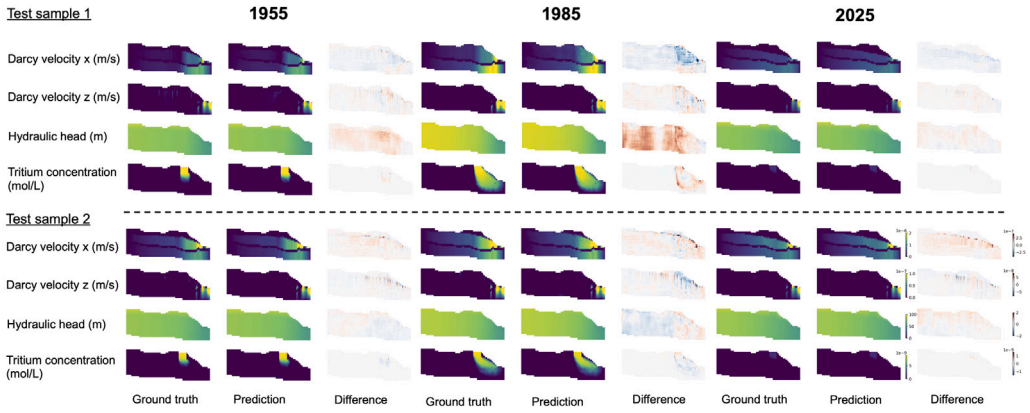

Fig. 8. Flow and transport properties predictions with U-FNOB-R, Index 9 in Table 2. The specific input parameters used for this sample, consisting of subsurface and climate variables, are detailed in the supplementary material Table S2.

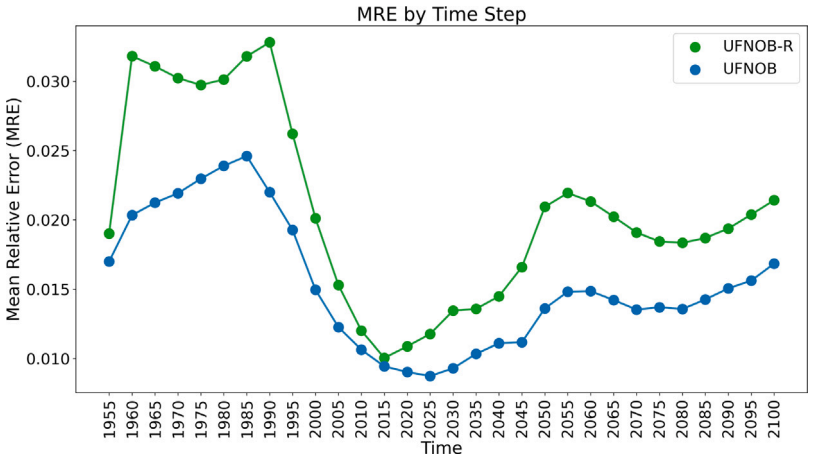

Fig. 9. Mean relative errors on test data over time for both U-FNOB and U-FNOB-R.

and tritium concentration. Utilizing our trained U-FNOB and U-FNOB-R models, we present predictions on two samples from the test data over time in Figs. 7 and 8. Detailed input parameters for these samples are provided in the Supplementary Material. Our predictions are found to be in close agreement with the ground truth obtained from physical simulations. However, some discrepancies are observed near plume boundaries and water tables. Overall, the results indicate that our approach is able to effectively capture the spatiotemporal variations of plumes and corresponding flow properties.

To further evaluate the performance of the U-FNOB and U-FNOB-R models, we calculate the MRE on test data (10% of our simulation dataset) over time (Fig. 9). The results show that the U-FNOB-R model has a larger MRE in general compared to the U-FNOB model. Additionally, we observe that the prediction errors of historical data are

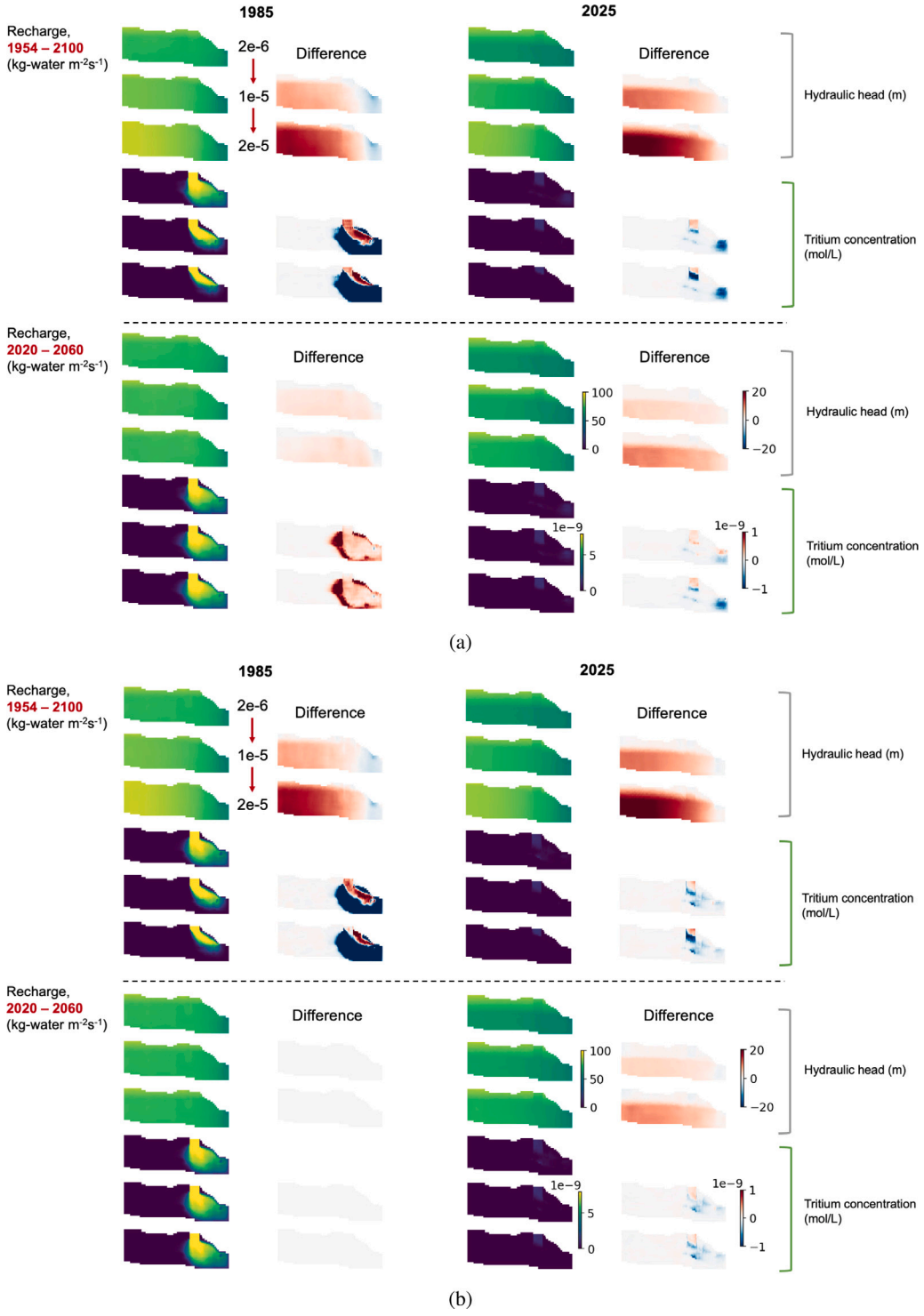

Fig. 10. Predictions with different recharge rates: differences on hydraulic head and tritium concentration after changing recharge rates for 150 years (1954–2020) or changing recharge rate for mid-century (2020–2060). (a) U-FNOB (b) U-FNOB-R. Differences are between 1e−5/2e−5 kg-water m^{-2} s^{-1} and 2e−6 kg-water m^{-2} s^{-1}. The test sample used for these simulations was derived from Table S2. The colorbar for hydraulic head and difference between hydraulic head, tritium concentration and difference between tritium concentration is in changing recharge rate for mid-century, 2025 comparison. Red means the value increases, blue means the value decreases, white means no change.

higher than those of future projections. Furthermore, the error of the U-FNOB-R model increases more significantly after the first time snapshot (1955) compared to the U-FNOB model. This discrepancy in error could be attributed to the use of two different U-FNOB-R models, one trained for the first time snapshot and one for the rest of the time snapshots, which may result in discrepancies that cannot be updated simultaneously.

3.6. Evaluating the reliance of groundwater contamination site to changing recharge rates

Climate change has the potential to induce severe precipitation occurrences and alterations in precipitation and evapotranspiration patterns, consequently affecting the infiltration process within the vadose zone and the recharge rate at groundwater contamination locations.

Projections of future precipitation and evapotranspiration are offered by global climate models, including CMIP5, but these forecasts are accompanied by a degree of uncertainty. In this section, we explore the adaptability of groundwater contamination sites in response to fluctuations in recharge rates, aiming to evaluate the possible consequences of climate change on these ecosystems. To test the climate resilience of the contamination sites, we manipulate the recharge rate from 2 $\times$ 10^{-6} kg-water m^{-2} s^{-1} to 1 $\times$ 10^{-5} and 2 $\times$ 10^{-5} kg-water m^{-2} s^{-1} (5$\times$ and 10$\times$ larger). We evaluate two scenarios: (1) changing recharge rates for only the mid-century (2020–2060) and (2) changing recharge rates for the entire period (1954–2100) on one test sample, specifically referring to the sample described in Table S2. Figs. 10(a) and 10(b) present differences in hydraulic head and tritium concentration with changing recharge rates.

In the first experiment, where we change recharge rates only for the mid-century (2020–2060), we find that U-FNOB (Fig. 10(a) bottom) has greater biases of hydraulic head and tritium concentrations at 1980, even when we keep the recharge rate before 2020 static. This behavior is unexpected since the model should be able to accurately capture the effects of changing recharge rates on the flow and transport properties. However, the U-FNOB-R architecture, as shown in Fig. 10(b), reasonably simulates the impacts by changing recharge rate and suggests that there is more remobilization near the source of the plume and more dilution for the downstream flow. Therefore, we prefer the U-FNOB-R architecture as it provides a more accurate time dependency between recharge rates and flow/transport properties.

In the second experiment, where we change recharge rates for nearly 150 years, we observe that higher recharge rates increase the hydraulic head on the upstream and decrease the hydraulic head on the downstream. Both U-FNOB (Fig. 10(a) top) and U-FNOB-R (Fig. 10(b) top) architectures show more remobilized contaminants near the capped area and more diluted solution near the plume boundary if recharge rates change from 2e−6 to 1e−5. However, if we increase recharge rates further from 1e−5 to 2e−5, the concentration increases are not as widespread and are more localized near the surface. This highlights the complexity of these physical systems to varying recharge rates, proving that our machine learning-based surrogate model is able to apply in climate resilience analysis.

The experimental results suggest that the U-FNOB-R architectural model provides a different perspective for projecting the influence of changes in recharge rate on groundwater contamination sites. One plausible explanation for this is that the U-FNOB-R architecture is Markovian, meaning that it only considers the immediate preceding time steps when making predictions. Conversely, the U-FNOB model encompasses the entire history of recharge rate changes. This nuanced difference in approaches brings about varying levels of complexity — the U-FNOB model's broader perspective may raise the risk of overfitting, which could potentially reduce the model's precision in predicting the effect of recharge rate changes on groundwater contamination sites.

4. Discussion and conclusions

In this study, machine learning methods, specifically U-FNOB and U-FNOB-R neural network architectures, were employed to model and predict transient flow and transport properties in groundwater systems based on physical simulation data. Building on the potential of machine learning, we developed efficient surrogate models that offer a less time-consuming and less expensive alternative to physical simulations. Implementing an additional U-Net architecture resulted in a significant decrease in the mean relative errors for both the FNO-2D and FNO-3D architectures, with the U-FNOB architecture demonstrating higher training efficiency. The inclusion of all data-driven and physical boundary constraints, such as spatial derivatives and no-flow conditions, further improved model accuracy.

On investigation of the impact of varying recharge rates, significant responses in the hydraulic head and tritium concentration were observed. This shows the sensitivity of subsurface systems to recharge rate changes and the U-FNOB-R architecture, which includes a recurrent network, accurately evaluated the impact of these variations. From a computational standpoint, as detailed in Section 3.4, our surrogate models displayed a substantial reduction in computational time compared to traditional forward model simulations. In terms of processing speed, the surrogate models outperformed traditional methods, demonstrating a more than 500-fold increase in speed. This significant improvement in efficiency showcases the potency of machine learning methodologies for practical applications.

The choice of architecture and loss function is pivotal to the performance of the surrogate models. With careful selection, our models can effectively predict system responses to changes in recharge rates while also saving substantial computational time once they are trained. This study emphasized a 2D spatial model with x and z directions but future work intends to implement the methodology on a 3D model. Though this will require greater computational resources and significantly more parameters for training, we are currently developing an efficient surrogate model for 3D flow and contaminant transport.

The insights generated from this study can be applied significantly in groundwater monitoring and remediation tasks, especially for sites like the Savannah River. The initial significant amount of data required for training these models is outweighed by the computational time and resources saved once the machine learning-based surrogate models are trained and operational.

CRediT authorship contribution statement

Aurelien Meray: Conceptualization, Methodology, Writing – original draft, Writing – review & editing, Visualization. **Lijing Wang:** Conceptualization, Methodology, Writing – original draft, Writing – review & editing, Visualization. **Takuya Kurihana:** Conceptualization, Methodology, Writing – review & editing. **Ilijana Mastilovic:** Conceptualization, Methodology, Writing – review & editing. **Satyarth Praveen:** Supervision, Writing – review & editing. **Zexuan Xu:** Supervision, Writing – review & editing. **Milad Memarzadeh:** Supervision, Writing – review & editing. **Alexander Lavin:** Supervision, Writing – review & editing. **Haruko Wainwright:** Supervision, Writing – review & editing.

Declaration of competing interest

The authors declare that they have no known competing financial interests or personal relationships that could have appeared to influence the work reported in this paper.

Data availability

The source codes are available at the link: https://console.cloud.google.com/storage/browser/us-digitaltwiner-pub-features/srs_farea_ensemble_simulations_dataset.

Acknowledgments

The present work was executed at the Frontier Development Laboratory (FDL) USA in 2022. FDL USA embodies a collaborative research initiative involving public and private organizations, including NASA, the SETI Institute, Trillium Technologies Inc, and a consortium of industry partners such as Google Cloud, Intel, IBM, Lockheed Martin, NVIDIA, and Pasteur Labs. These entities contribute critical data, expertise, training, and computational resources that facilitate rapid experimentation and iteration in data-intensive domains. The current material is based on research supported by the Department of Energy, United States of America's Artificial Intelligence & Technology Office under Award Number DE-AI0000001. Furthermore, this investigation is backed by the U.S. Department of Energy's Office of

Environmental Management through the Advanced Long-term Monitoring Systems (ALTEMIS) project. Funding was granted under Award Number DE-AC02-05CH11231 to Lawrence Berkeley National Laboratory, United States of America. The research made use of the National Energy Research Scientific Computing Center (NERSC) resources, a U.S. Department of Energy Office of Science User Facility situated at Lawrence Berkeley National Laboratory, operating under contract DE-AC02-05CH11231. In addition, the study utilized the Lawrencium computational cluster resource provided by the IT Division at Lawrence Berkeley National Laboratory, which received support from the Director of the Office of Science, United States of America and the Office of Basic Energy Sciences within the U.S. Department of Energy under contract DE-AC02-05CH11231.

Code availability

Name of code: U-FNOB Year first available: 2023 Contact: amera009@fiu.edu Program language: Python 3.7 Software required: PyTorch 1.11 Program size: 12 MB. The source codes are available for download at the link: https://github.com/ALTEMIS-DOE/U-FNOB

Appendix A. Supplementary data

Supplementary material related to this article can be found online at https://doi.org/10.1016/j.cageo.2023.105508.

References

Bea, S.A., Wainwright, H., Spycher, N., Faybishenko, B., Hubbard, S.S., Denham, M.E., 2013. Identifying key controls on the behavior of an acidic-U (VI) plume in the savannah river site using reactive transport modeling. J. Contam. Hydrol. 151, 34–54.

Clement, T.P., Truex, M.J., Lee, P., 2002. A case study for demonstrating the application of US EPA's monitored natural attenuation screening protocol at a hazardous waste site. J. Contam. Hydrol. 59 (1–2), 133–162.

Denham, M.E., Amidon, M.B., Wainwright, H.M., Dafflon, B., Ajo-Franklin, J., Eddy-Dilek, C.A., 2020. Improving long-term monitoring of contaminated groundwater at sites where attenuation-based remedies are deployed. Environ. Manag. 66 (6), 1142–1161.

Desimone, L.A., McMahon, P.B., Rosen, M.R., et al., 2014. Water Quality in Principal Aquifers of the United States, 1991–2010. US Department of the Interior, US Geological Survey.

Haghighat, E., Amini, D., Juanes, R., 2022. Physics-informed neural network simulation of multiphase poroelasticity using stress-split sequential training. Comput. Methods Appl. Mech. Engrg. 397, 115141.

He, Q., Tartakovsky, A.M., 2021. Physics-informed neural network method for forward and backward advection-dispersion equations. Water Resour. Res. 57 (7), e2020WR029479.

Hendrycks, D., Gimpel, K., 2016. Bridging nonlinearities and stochastic regularizers with Gaussian error linear units. CoRR abs/1606.08415. arXiv:1606.08415. URL: http://arxiv.org/abs/1606.08415.

Katz, R.W., Brown, B.G., 1992. Extreme events in a changing climate: variability is more important than averages. Clim. Change 21 (3), 289–302.

Knutti, R., Sedláček, J., 2013. Robustness and uncertainties in the new CMIP5 climate model projections. Nat. Clim. Change 3 (4), 369–373.

Lavin, A., Zenil, H., Paige, B., Krakauer, D.C., Gottschlich, J.E., Mattson, T.G., Anandkumar, A., Choudry, S., Rocki, K., Baydin, A.G., Prunkl, C., Isayev, O., Peterson, E.J., McMahon, P.L., Macke, J.H., Cranmer, K., Zhang, J., Wainwright, H.M., Hanuka, A., Veloso, M.M., Assefa, S.A., Zheng, S., Pfeffer, A., 2021. Simulation intelligence: Towards a new generation of scientific methods. ArXiv abs/2112.03235.

Li, Z., Kovachki, N., Azizzadenesheli, K., Liu, B., Bhattacharya, K., Stuart, A., Anandkumar, A., 2020. Fourier neural operator for parametric partial differential equations. arXiv preprint arXiv:2010.08895.

Li, Z., Zheng, H., Kovachki, N., Jin, D., Chen, H., Liu, B., Azizzadenesheli, K., Anandkumar, A., 2021. Physics-informed neural operator for learning partial differential equations. arXiv preprint arXiv:2111.03794.

Libera, A., de Barros, F.P., Faybishenko, B., Eddy-Dilek, C., Denham, M., Lipnikov, K., Moulton, D., Maco, B., Wainwright, H., 2019. Climate change impact on residual contaminants under sustainable remediation. J. Contam. Hydrol. 226, 103518.

Lu, L., Jin, P., Karniadakis, G.E., 2019. Deeponet: Learning nonlinear operators for identifying differential equations based on the universal approximation theorem of operators. arXiv preprint arXiv:1910.03193.

Mackay, D.M., Cherry, J.A., 1989. Groundwater contamination: Pump-and-treat remediation. Environ. Sci. Technol. 23 (6), 630–636.

Meray, A.O., Sturla, S., Siddiquee, M.R., Serata, R., Uhlemann, S., Gonzalez-Raymat, H., Denham, M., Upadhyay, H., Lagos, L.E., Eddy-Dilek, C., et al., 2022. PyLEnM: A machine learning framework for long-term groundwater contamination monitoring strategies. Environ. Sci. Technol. 56 (9), 5973–5983.

Nyer, E.K., 2000. In Situ Treatment Technology. CRC Press.

Orlowsky, B., Seneviratne, S.I., 2012. Global changes in extreme events: regional and seasonal dimension. Clim. Change 110 (3), 669–696.

Rahmstorf, S., Coumou, D., 2011. Increase of extreme events in a warming world. Proc. Natl. Acad. Sci. 108 (44), 17905–17909.

Raissi, M., Perdikaris, P., Karniadakis, G.E., 2019. Physics-informed neural networks: A deep learning framework for solving forward and inverse problems involving nonlinear partial differential equations. J. Comput. Phys. 378, 686–707.

Ronneberger, O., Fischer, P., Brox, T., 2015. U-net: Convolutional networks for biomedical image segmentation. In: Medical Image Computing and Computer-Assisted Intervention–MICCAI 2015: 18th International Conference, Munich, Germany, October 5-9, 2015, Proceedings, Part III 18. Springer, pp. 234–241.

Schmidt, F., Wainwright, H.M., Faybishenko, B., Denham, M., Eddy-Dilek, C., 2018. In situ monitoring of groundwater contamination using the Kalman filter. Environ. Sci. Technol. 52 (13), 7418–7425.

Wen, G., Li, Z., Azizzadenesheli, K., Anandkumar, A., Benson, S.M., 2022. U-FNO—An enhanced Fourier neural operator-based deep-learning model for multiphase flow. Adv. Water Resour. 163, 104180.

Xu, Z., Serata, R., Wainwright, H., Denham, M., Molins, S., Gonzalez-Raymat, H., Lipnikov, K., Moulton, J.D., Eddy-Dilek, C., 2022. Reactive transport modeling for supporting climate resilience at groundwater contamination sites. Hydrol. Earth Syst. Sci. 26 (3), 755–773.

Zhang, K., Zuo, Y., Zhao, H., Ma, X., Gu, J., Wang, J., Yang, Y., Yao, C., Yao, J., 2022. Fourier neural operator for solving subsurface oil/water two-phase flow partial differential equation. SPE J. 1–15.